(Received 22 August 2023, Accepted 26 December 2023, Scheduled 29 December 2023)

Full-Wave Electromagnetic Simulations of Forests at L-Band by Using Fast Hybrid Method

Jongwoo Jeong[1,*], Leung Tsang[1], Andreas Colliander[2], and Simon Yueh[2]

[1] *Electrical Engineering and Computer Science, University of Michigan, Ann Arbor, MI 48105, USA*
[2] *Jet Propulsion Laboratory, California Institute of Technology, Pasadena, CA 91109, USA*

ABSTRACT: Wave propagation in forests at L-band has essential applications in satellite communication system design, foliage penetration (FOPEN), and remote sensing of forest canopy and soil using passive active and reflectometry techniques. In this work, we propose applying the fast hybrid method (FHM) for full-wave simulations of forests. The FHM significantly improves CPU time and memory efficiency for full-wave electromagnetic solutions. In this paper, we present simulations of forests of up to 72 trees with heights up to 13 m with FHM. Spatial distributions of electric fields at the bottom plane of the trees are illustrated showing constructive and destructive interferences. The electric field distributions show that the amplitudes of the electric fields can be as large as twice that of incident waves. The transmissivities are computed and averaged over realizations based on the electric fields underneath the forest. The simulations were performed on a desktop and required a CPU time of only 1346 seconds and the memory of 16.5 GB for the case of 72 13-m tall trees, demonstrating that the FHM method is substantially more efficient than the available commercial software. The results show that the L-band signals can penetrate forests to sense the soil moisture and detect targets hidden within forests, as evidenced by significant electric field intensities under forest canopies. Also, we illustrate that GPS signals can penetrate forests and be successfully received by GPS receivers. In the study on clustering effects, we present two distinct solutions for transmissivities, each corresponding to different spatial distributions of trees while maintaining the same average tree density.

1. INTRODUCTION

Microwave propagation through forests is an important problem as forests cover 1/3 of the land surface. For accurate analyses of wave propagation through forests, full-wave electromagnetic simulations are preferred in many applications. First, with the rapid advancement of satellite communication, channel modeling of forested environments is essential in communication system. Designing and optimizing wireless systems in forest environments requires the electromagnetic characterization of forests [1–3]. A second application of radio signal penetration through forests is foliage penetration (FOPEN) [4–8]. Since forest canopies attenuate the radio signals and give clutter scattering, electromagnetic wave models of forest can provide critical information for FOPEN. The third application is microwave remote sensing of soil moisture biomass, and vegetation water content (VWC). Microwave remote sensing at L-band (1.4 GHz) is utilized by the SMAP (Soil Moisture Active Passive) mission, aiming at a global mapping of soil moisture [9, 10], the NISAR (National Aeronautics and Space Administration and Indian Space Research Organization Synthetic Aperture Radar), the reflectometry missions CYGNSS (Cyclone Global Navigation Satellite System) and HydroGNSS [11–16]. To extend the scope of the SMAP mission to include forested areas that have VWC much more than 5 kg/m^2 (the original VWC threshold of the mission for validated soil moisture retrieval [17]), it is imperative to develop an electromagnetic model that can assess the impact of trees and accurately characterize the interaction between electromagnetic waves and trees.

In the past, electromagnetic modeling of trees often relied on the radiative transfer equation (RTE) and the distorted Born approximation (DBA) [18, 19]. As discussed in [18], the RTE model has several adhoc assumptions. In particular the RTE model assumes a uniform, random distribution of scatterers throughout the forest canopy. This assumption requires that the leaves, the branches and then trunks are uniformly randomly positioned. Another way to express the assumption of uniform randomness in position is that RTE results of different spatial distributions of scatterers will be the same if the average number of scatterers is the same. On the other hand, Maxwell equations will give different results for uniform randomly positioned scatterers and scatterers in clusters even though the two cases have the same average number of scatterers. Also, forest geometric configurations have gaps among trees. The gaps are the leaves of different trees, between branches of different trees, and between trunks of different trees. The gaps allow more penetration of electromagnetic waves [20]. To consider the effects of gaps in electromagnetic propagation, we use full-wave solutions that include many trees in electromagnetic models [21]. Many trees need to be used in the simulation area to capture the multiple scattering effects and the effects of gaps. However, using commercial software for full-wave simulations involving numerous scatterers is constrained by CPU time and memory limitations: a simulation of 9 corn plants on the commercial software (HFSS) already exceeded the memory capacity [22].

* Corresponding author: Jongwoo Jeong (jjongwoo@umich.edu).

TABLE 1. Comparisons of sizes of problems for L-band corn field, P-band forests, and L-band forests.

	L-band, corns (1.41 GHz) wavelength = 0.21 m	**P-Band, trees (370 MHz) wavelength = 0.81 m**	**L-Band, trees (1.41 GHz) wavelength = 0.21 m**
H **(height)**	5.9λ (1.25 m)	19.7λ (16 m)	61λ (13 m)
$\boldsymbol{L^2}$ **(area)**	$2 \cdot 10^3\lambda^2$ ($91.0\,\mathrm{m}^2$)	$1.95 \cdot 10^3\lambda^2$ ($1281.6\,\mathrm{m}^2$)	$1.58 \cdot 10^4\lambda^2$ ($714\,\mathrm{m}^2$)
$\boldsymbol{HL^2}$ **(volume)**	$0.12 \cdot 10^5\lambda^3$ ($113.8\,\mathrm{m}^3$)	$0.38 \cdot 10^5\lambda^3$ ($20{,}506.0\,\mathrm{m}^3$)	$\mathbf{*9.64 \cdot 10^5\lambda^3}$ ($9{,}282\,\mathrm{m}^3$)

*This large-scale problem has not been solved before.

To obtain accurate and efficient full-wave solutions for trees, we began full wave simulations in [23] and the hybrid method (HM) was proposed later in [24]. The initial HM in [24] assumes that the dominant contribution to the scattered waves comes from the tree trunks, which enables the scattering solutions of a single dielectric cylinder using the Infinite Cylinder Approximation (ICA). The analytical wave scattering solutions provide the T-matrix formulation of a single tree, which is then used to derive the Foldy-Lax equation for calculating the interactions among trees. This approach can provide scattering solutions for up to 196 trees. In [24], the illustrated examples consider dielectric cylinders that are randomly and uniformly distributed. Despite being able to solve the wave scattering of trunk-dominant trees in [24], the initial hybrid method still faces challenges regarding CPU time and memory, particularly as the height of the trees increases and the number of T-matrix elements grows. Therefore, in our subsequent papers, the hybrid method heavily relied on high-performance computing (HPC) with parallel processing [20, 21, 24, 25].

However, the assumption of trunk-dominant trees may not hold for many real forest geometries. A tree consists of a trunk, primary branches, and several levels of secondary branches. There are also trees where the trunks are considerably shorter than the overall tree height, with branches rapidly extending from the trunk. The electromagnetic model should include branch contributions from each tree because they affect the scattering solutions at L-band frequency (1.41 GHz). This led to the development of the hybrid method [25]. The concept of the HM is to extract the T-matrix of a single tree with the aid of commercial software. Available commercial software can compute electromagnetic fields of trees with complex geometries, which are used to extract the T-matrix components from bistatic scattering solutions of a single tree. However, to consider the multiple scattering among many trees, the HM necessitates using an HPC cluster with large memory and CPUs with 36 parallel processors As the number of trees increases in the HM, the computational complexity and memory grows with $O(N^2)$. Considering that a tree height is proportional to the z-directional wave vector component in modal expansion, this further increases the computational complexity. Also, the demands of full-wave simulations are frequency dependent with higher frequency requiring a larger number of vector wave functions. Since wave scattering simulation for random media requires multiple realizations to obtain the convergent remote sensing parameters [24], fast electromagnetic solutions are necessary to complete the simulations efficiently so that results of look up tables can be generated rapidly for users.

This motivates the further development of the hybrid method, leading to the fast hybrid method (FHM), the fast version of the hybrid method [22]. To improve CPU time and memory usage, the FHM combines the 2D sparse matrix canonical grid (SMCG) FFTs [26] and 1D FFT for spatial domain and orders of cylindrical wave functions, respectively. This approach involves the computation of the Foldy-Lax equation using a "triple FFT" technique. The FHM utilizes a three-step approach, involving (i) the extraction of T-matrix for a tree in vector cylindrical waves (VCW), (ii) the formulation of Foldy-Lax multiple scattering in VCW and (iii) the implementation of fast multiple scattering solutions based on triple FFT.

The computational complexity of the FHM results in significant reductions in CPU time, with a computational complexity of $O(N \log N)$ and memory usage of $O(N)$. This allows the scattering solutions of 72 trees within a CPU time of 1346 seconds and memory of 16.5 GB on a standard desktop without needing a HPC cluster. The FHM was previously applied to the corn field at the L-band [22] and forests at the P-band [27]. Forests at the L-band are much more challenging because the tree dimensions are much larger than the corn dimensions, and the L-band wavelength is smaller (four times smaller in these examples) than the P-band wavelength. The sizes of the three problems are compared in Table 1. The present problem of L-band forests is much larger than the previous two problems. In particular, the forest problem in this paper is 82 times larger than the previous corn problem as seen in the last row of Table 1.

The full-wave simulations provide solutions that correspond to specific geometric configurations. This means that the different distributions of trees result in different transmissivities, whereas the RTE only provides one transmissivity since it uses the constant n_0 in its governing equation [23]. In [24], the full-wave simulation includes a medium with trees uniformly distributed, and these trees possess dominant trunks, aligning with the RTE assumption. However, this may not be true because the

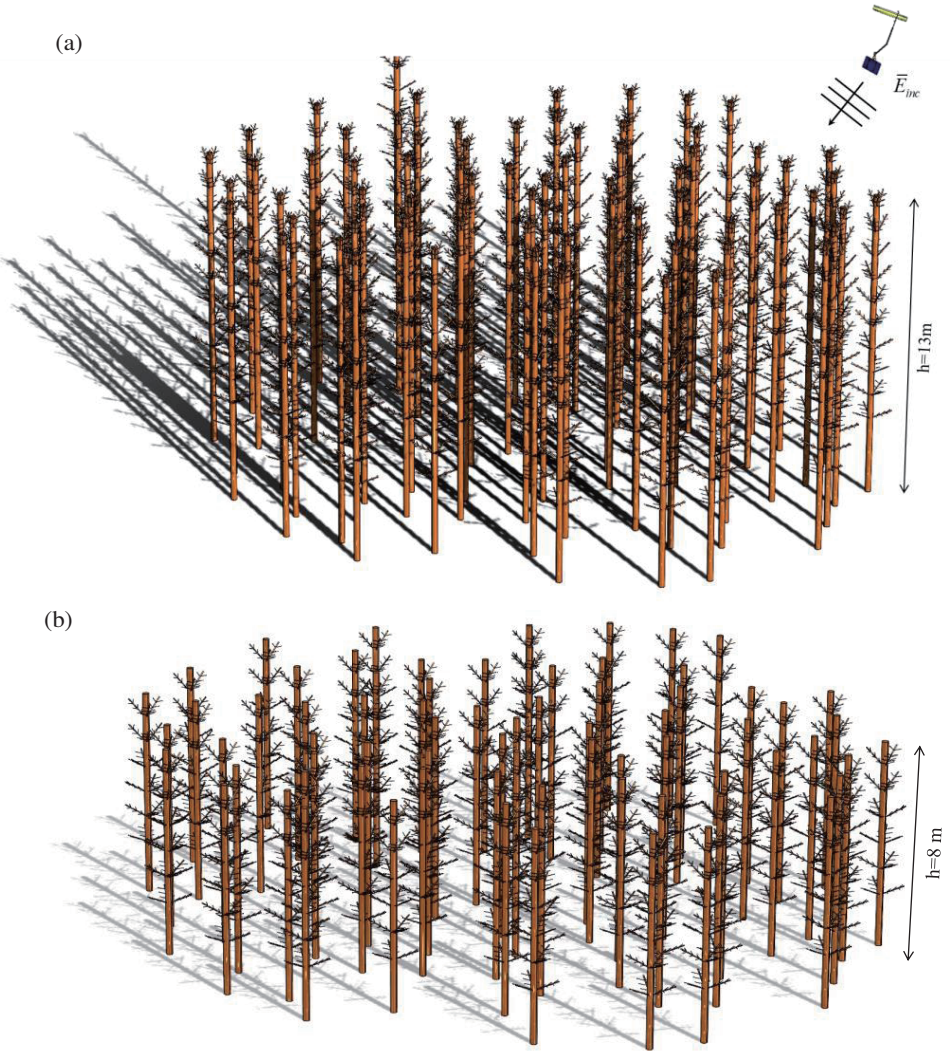

FIGURE 1. Geometric configuration of 72 trees: (a) Forest of 13 m trees (b) eight m trees.

trunk may not be dominant and the trees can be non-uniformly positioned.

This paper applies the FHM for efficient full-wave electromagnetic simulations of forests at the L-band. The forests consist of 8 m and 13 m trees as shown in Figs. 1(a) and (b), which encompass a total of 72 trees spanning an area of 714 m^2. We analyze the spatial distributions of electric fields underneath the forest, revealing three physical results: (a) Field distributions at the bottom plane of the trees demonstrated significantly higher maximum amplitudes compared to the incident waves. Furthermore, the electric field distributions vary across the forest, with variations depending on whether the field points were located in shadowed regions or gaps between trees. (b) Transmissivities computed by averaging the reception area and averaging over realizations are found to be significantly higher than those predicted by the RTE [21]. (c) To account for the effects of the geometric configuration we apply the FHM to the non-uniform (tree clusters) and uniform distributions of trees, resulting in distinct transmissivity results.

In applications, the paper addresses three questions: (a) Can L-band signal penetrate forests to see soil moisture? (b) Can L-band penetrate forests and detect target hidden inside the forests? (c) Can GPS signals penetrate the forests and be received by GPS receivers? For microwave remote sensing, the fullwave simulations show that the L-band signals can penetrate the forests and sense the soil moisture below. Previously, the NASA SMAP satellite mission had an upper threshold for the volumetric water content of vegetation, limited to 5 kg/m^2. For the forests at L-band, the full-wave simulations use VWC $> 13.46\,kg/m^2$ much larger than the previous threshold. As a result of these new findings of fullwave simulations, a new phase of the SMAP mission, known as the extended mission, has begun. Several ground and airborne campaigns have been conducted in Massachusetts, New York and Canada. Future campaigns are planned for rain forests in Asia. For hidden target detection, we illustrate the spatial distribution of the electric fields in the plane below the forests. The results show spatial electric field patterns with significant field strength which are useful for the hidden target detection under forests. For

GPS communications, the results show that the received electric fields can be twice that of the incident wave due to constructive interference and gap effects while the field strength is smaller than the incident wave in the shadow region. The full-wave simulation results show the possibility of GPS signal reception under forests.

There are several studies on full-wave simulations for cylinders or multi-scatterers. In [28], the simulation applies the method of auxiliary sources and focuses on a trunk-dominant tree in a 2-D problem. In reality, trees consist of branches connected to the trunk with complex-shapes. Moreover, microwaves in forests come from above, typically via satellite, whereas [28] is limited to lateral wave propagations. In [29], a full-wave simulation was conducted using the source-model technique accelerated by the Fast Multipole Method (FMM). However, considering an electrically large height of trees (61λ) and nearly 72 scatterers, it is unsuitable for addressing forest-related issues due to the computational complexity approaching $O(N^{1.5})$, where N is proportional to the number of source points. Additionally, scatterers with dielectric mediums have not been considered yet. The present FHM method is much more efficient than FEKO which is an FMM based method.

In addition to applying RTE, ray tracing methods have been utilized. The method is designed for applications with high frequencies, such as for millimeter waves [30]. However, at L-band, forests have multiscale features of scatterers and gaps ranging from larger than the wavelength to comparable to the wavelength to smaller than the wave length. Thus, the ray tracing method is not valid at L-band.

The paper is organized as follows. In Section 2, we provide an overview of the three steps involved in the FHM process. This includes a detailed description of the T-matrix extraction approach for vector cylindrical waves (VCWs) and the implementation of fast-multiple scattering solutions derived from the Foldy-Lax equation. Section 3 discusses the transmissivity computation with the simulation design of the forest and its verification. In Section 4, electric fields and transmissivities of 72 trees are illustrated for 8 m trees and 13 m trees, respectively. To accommodate mixed-height trees, forests of a combinations of 8 m and 13 m trees are also considered. Using a cluster of trees, we show that full-wave simulations yield different solutions for trees distributed uniformly and those clustered together, even when the average densities remain the same.

2. FULL-WAVE ELECTROMAGNETIC SIMULATION BY FAST HYBRID METHOD

Performing full-wave simulations of wave scattering from forests comprising many trees is a highly complex task requiring many computational operations. To effectively express the multiple scattering of electromagnetic waves with trees, modal expansion has proven to be advantageous [31]. Modal expansion represents the electromagnetic waves using vector wave functions with a set of expansion coefficients. By employing vector wave functions, the computation of wave scattering is greatly simplified, facilitating the linear addition of orthogonal wave functions. Among the different vector wave functions available, VCWs are well-suited for wave scattering of forests. This is primarily because the smallest enclosing cylinder of a tree used in the T-matrix extraction can be densely positioned on the x-y plane when we consider tree heights are typically larger than the maximum radii of the trees. Previously, multiple scattering was usually studied with vector spherical wave (VSW) expansions. However, the smallest enclosing sphere of a tree in vector spherical waves is the diameter of the sphere equal to the tree's height. This would prevent the enclosing spheres from being located in close proximity to one another. Therefore, using VCWs instead of VSWs allows a more efficient representation of wave scattering in forests, considering the various spatial arrangements and dimensions of the trees involved.

2.1. Novelty of the FHM

The FHM procedure consists of three steps. The first step is extracting the T-matrix using commercial software such as FEKO, HFSS, and CST [32]. Using plane waves incidences in commercial software, the bistatic scattering amplitudes are then used to determine the T-matrix elements by matching to the far-field solutions of VCWs. In the second step, the multiple scattering solutions of the Foldy-Lax equation based on VCWs are formulated to find electromagnetic interaction among trees. The Foldy-Lax equations are then solved iteratively to obtain orders of the numerous scattering solutions. The ultimate step involves applying a triple FFT process to each order of the multiple scattering solutions, thereby substantially mitigating the computational complexity.

T-matrix represents characteristics of the wave scattering by a single scatterer. In modeling forests, we treat an entire tree as a single scatterer. This is different from previous RTE modeling that each branch, each leaf and each trunk are treated as single scatterers. In VCWs, the T-matrix elements relate incident waves to scattered waves outside an enclosing cylinder of a single tree. Electric fields are represented by TE (horizontal polarization), $\bar{M}$ and TM (vertical polarization), $\bar{N}$ modes of vector cylindrical wave functions. The exciting waves can be expressed using the following equation [31],

$$\bar{E}^{ex}(\bar{r}) = \sum_n \int_{-k}^{k} dk_z \left[a_n^{EM}(k_z)\, Rg\bar{M}_n(k_z,\bar{r}) + a_n^{EN} Rg\bar{N}_n(k_z,\bar{r}) \right] \quad (1)$$

where

$$Rg\bar{M}_n(k_z,\bar{r}) = \left[\hat{\rho}\frac{in}{\rho} J_n(k_\rho\rho) - \hat{\phi} k_\rho J_n'(k_\rho\rho) \right] e^{ik_z z + in\phi},$$

$$Rg\bar{N}_n(k_z,\bar{r}) = \left[\hat{\rho}\frac{ik_\rho k_z}{k} J_n'(k_\rho\rho) - \hat{\phi}\frac{nk_z}{k\rho} J_n(k_\rho\rho) + \hat{z}\frac{k_\rho^2}{k} J_n(k_\rho\rho) \right] \times e^{ik_z z + in\phi}.$$

"Rg" denotes regular functions, which use Bessel functions An approximation is made in (1), where the integration over k_z is limited to propagating waves, as the contribution of evanescent

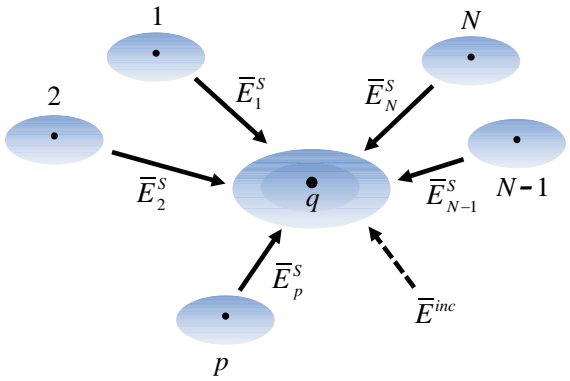

FIGURE 2. Final excitation fields acting on scatterer q in Foldy-Lax equation.

waves from one tree to another is neglected (We are presently studying the inclusion of evanescent waves components) For scattered waves Hankel functions of the first kind (without "Rg") are used as shown below,

$$\bar{E}^s(\bar{r}) = \sum_n \int_{-k}^{k} dk_z \left[a_n^{SM}(k_z)\bar{M}_n(k_z,\bar{r}) + a_n^{SN}\bar{N}_n(k_z,\bar{r})\right]. \quad (2)$$

The T-matrix gives the relationship between the exciting wave coefficients in (1) and the scattered wave coefficients in (2) as the following

$$\begin{aligned} a_n^{SM}(k_z) &= \sum_{n'}\int_{-k}^{k} dk_z' \\ &\times \left[T_{nn'}^{MM}(k_z,k_z')\,a_{n'}^{EM}(k_z') + T_{nn'}^{MN}(k_z,k_z')\,a_{n'}^{EN}(k_z')\right], \\ a_n^{SN}(k_z) &= \sum_{n'}\int_{-k}^{k} dk_z' \\ &\times \left[T_{nn'}^{NM}(k_z,k_z')\,a_{n'}^{EM}(k_z') + T_{nn'}^{NN}(k_z,k_z')\,a_{n'}^{EN}(k_z')\right]. \end{aligned} \quad (3)$$

As discussed in [34], the T-matrix can be extracted by employing the far-field solutions, as the VCW expansions of the scattered waves are valid in the entire domain outside of the enclosing cylinder for both near fields and far fields. By taking a double Fourier series over the scattering amplitudes of a single scatterer in commercial software, the T-matrix elements can be extracted from the bistatic polarimetric scattering amplitudes as follows [22, 34]:

$$\begin{aligned} &T_{nn'}^{(\alpha,\beta)}(k\cos\theta_s, k\cos\theta_i) \\ &= \frac{\xi_{\alpha,\beta}\sin\theta_i}{8\pi^2\sin\theta_s} i^{n-n'} \int_0^{2\pi} d\phi_s \int_0^{2\pi} d\phi_i e^{i(n'\phi_i - n\phi)} \\ &\times f_{\alpha\beta}(\theta_s,\phi_s;\theta_i,\phi_i), \end{aligned} \quad (4)$$

where α and β correspond to either **M** or **N** vector cylindrical functions, which indicate $\xi_{\alpha,\beta}$ and $f_{\alpha\beta}$ as

$\xi_{\alpha,\beta}$ value

α/β	M	N
M	i	1
N	-1	i

$f_{\alpha\beta}$

α/β	M	N
M	f_{hh}	f_{hv}
N	f_{vh}	f_{vv}

In (4), $f_{\alpha\beta}$ is bistatic polarimetric scattering amplitude, where subscripts "s" and "i" mean scattered and incident waves, respectively. We have also used the transformations $k_z = k\cos\theta$. Note that physical rotation of trees along azimuthal angles can be calculated by coordinate transformation of the T-matrix. However, the shapes of the trees do not exhibit remarkable variations with azimuthal angles. The computed T-matrices of single trees with different sizes and orientations can be stored in a library and are reused for multiple scattering simulations in various scenarios.

Using the Foldy-Lax equation, we can formulate multiple scattering solutions. The Foldy-Lax equation states that the excitation fields acting on a scatterer q can be represented as the sum of the incident waves and the scattered waves generated by the other scatterers as shown in Fig. 2. This can be expressed in the equation below,

$$\bar{E}_q^{ex}(\bar{r}) = \bar{E}^{inc}(\bar{r}) + \sum_{p=1,p\neq q}^{N} \bar{E}_{qp}^{s}(\bar{r}) \quad (5)$$

where $\bar{E}_q^{ex}(\bar{r})$ is the final excitation field acting on q. In this formulation each scatterer is represented by an index q corresponding to an entire tree. The positions of the tree in the horizontal plane are expressed as a 2-D vector $\bar{\rho}_q = x_q\hat{x} + y_q\hat{y}$. The positions are random (non-periodic). Substituting (1) and (2) into (5), the electric fields are expanded in VCWs as

$$\begin{aligned} &\sum_n \int_{-k}^{k} dk_z \left[a_n^{EM,(q)}(k_z) Rg\bar{M}_n(k_z,\bar{r}) + a_n^{EN,(q)} Rg\bar{N}_n(k_z,\bar{r})\right] \\ &= a_n^{M,inc}(k_{iz})\,Rg\bar{M}_n(k_{iz},\bar{r}) + a_n^{N,inc}(k_{iz})\,Rg\bar{N}_n(k_{iz},\bar{r}) \\ &+ \sum_{p=1,p\neq q}^{N}\sum_n \int_{-k}^{k} dk_z \left[a_n^{SM}(k_z)\bar{M}_n(k_z,\bar{r}) + a_n^{SN}\bar{N}_n(k_z,\bar{r})\right] \end{aligned} \quad (6)$$

where the coefficients of incident planewaves [31] are

$$a_n^{M,inc}(k_{iz}) = \frac{i^{n+1}e^{-in\phi_i}}{k_{i\rho}} E_{hi}\delta(k_z - k_{iz}),$$

$$a_n^{N,inc}(k_{iz}) = \frac{i^{n}e^{-in\phi_i}}{k_{i\rho}} E_{vi}\delta(k_z - k_{iz}).$$

Applying the translation addition theorem, (6) is rearranged in terms of regular wave functions. The translation addition theorem enables the transformation from an outgoing wave from scatterer p to a linear combination of incoming waves on scatterer q as shown below [25, 31],

$$\begin{aligned}
&\bar{M}_n(k_z, k_\rho|\bar{\rho}-\bar{\rho}_p|)\\
&=\sum_{n'}^{\infty} Rg\bar{M}_{n'}(k_z, \bar{\rho}-\bar{\rho}_q) H_{n'-n}(k_\rho|\bar{\rho}_p-\bar{\rho}_q|)\\
&\times \exp\left(-i(n'-n)\phi_{\overline{\rho_p\rho_q}}\right)\exp(-ik_z(z_p-z_q)),\\
&\bar{N}_n(k_z, k_\rho|\bar{\rho}-\bar{\rho}_p|)\\
&=\sum_{n'}^{\infty} Rg\bar{N}_{n'}(k_z, \bar{\rho}-\bar{\rho}_q) H_{n'-n}(k_\rho|\bar{\rho}_p-\bar{\rho}_q|)\\
&\times \exp\left(-i(n'-n)\phi_{\overline{\rho_p\rho_q}}\right)\exp(-ik_z(z_p-z_q)).
\end{aligned} \tag{7}$$

On the substitution of (7) into (6) with the discretized k_z and changing excitation coefficients with scattering coefficients [22], we obtain the following matrix form of the Foldy-Lax equations

$$\begin{pmatrix} \psi^{SM} \\ \psi^{SN} \end{pmatrix} = \begin{pmatrix} I - F^{MM} & -F^{MN} \\ -F^{NM} & I - F^{NN} \end{pmatrix} \begin{pmatrix} a^{SM} \\ a^{SN} \end{pmatrix} \tag{8}$$

where

$$\begin{aligned}
&F^{\beta,\alpha}_{qm',pn}(k_{z,n_z}, k'_{z,n_z})\\
&=\sum_m T^{(\beta,\alpha),q}_{m'm}(k_{z,n_z}, k'_{z,n_z})\sigma^{qp}_{mn}(k'_{z,n_z}),
\end{aligned}$$

$$\sigma^{qp}_{mn}(k_{z,n_z}) = \begin{cases} \Delta k_z H^{(1)}_{m-n}(k_{\rho,n_z}|\bar{\rho}_p-\bar{\rho}_q|) \\ \exp\left(-i(m-n)\phi_{\overline{\rho_p\rho_q}}\right) \\ \exp(-ik_{z,n_z}(z_p-z_q)), \ \text{for } q\neq p \\ 0, \ \text{for } q=p, \end{cases}$$

$$\begin{aligned}
\psi^{S,\beta}_{qm'}(k_{z,n_z}) &= \sum_m \exp(i\bar{k}_i\cdot\bar{r}_q)\frac{i^m\exp(-im\phi_i)}{k_{i\rho}}\\
&\times\left[iE_{hi}T^{(\beta,M)}_{m'm,q}(k_{z,n_z}, k_{iz}) - E_{vi}T^{(\beta,N)}_{m'm,q}(k_{z,n_z}, k_{iz})\right],
\end{aligned}$$

$\alpha, \beta \in \{M, N\}$ and n_z is an index of the discretized k_z. It is interesting to observe that T-matrices are embedded in the Foldy-Lax equation when expressed in VCWs. Once extracted in the step 1, the T-matrices are reused many times in the Foldy Lax equations of (8). The system of linear equations in (8) is solved using an iterative approach as described in [21, 22, 35],

$$\mathbf{a^S} = \boldsymbol{\psi_S} + \mathbf{F}\boldsymbol{\psi_S} + \mathbf{F}^2\boldsymbol{\psi_S} + \cdots + \mathbf{F}^{n-1}\boldsymbol{\psi_S} \tag{9}$$

where $\mathbf{F}$ and ψ_S consist of the sub-matrices $\mathbf{F}^{\beta\alpha}$, $\boldsymbol{\psi}^{SM}$ and $\boldsymbol{\psi}^{SN}$, respectively. The scattering coefficients can be obtained efficiently by iteratively applying the Foldy-Lax matrix until convergence Each term in (9) corresponds to an order of multiple scattering with $\boldsymbol{\psi_S}$ as the first order, $\mathbf{F}\boldsymbol{\psi_{inc}}$ as the second order, $\mathbf{F}^2\boldsymbol{\psi_{inc}}$ as the third order, and $\mathbf{F}^{n-1}\boldsymbol{\psi_S}$ as the n-th order scattered fields.

As discussed in [22], the computational bottleneck in (8) arises from the product of $\mathbf{F}$ with a column vector. This involves the computation of translation addition terms such as $\sigma^{qp}_{mn}(k_{z,n_z})\, a_n^{S\alpha}(k_{z,n_z})$. To improve the computational complexity, a triple FFT form is formulated by substituting the positions of the scatterers p and q

$$\begin{aligned}
|\bar{\rho}_p-\bar{\rho}_q| &= \sqrt{\Delta x^2\left(\alpha'_g-\alpha_g\right)^2 + \Delta y^2\left(\beta'_g-\beta_g\right)^2},\\
\phi_{\overline{\rho_p\rho_q}} &= \tan\left(\Delta y\left(\beta'_g-\beta_g\right)/\Delta x\left(a'_g-\alpha_g\right)\right)
\end{aligned} \tag{10}$$

into (8). α', β' correspond to the scatter q and α, β correspond to the scatterer p, respectively. Applying 2D-SMCG FFTs to $\sigma^{qp}_{mn}(k_{z,n_z})\, a_n^{S\alpha}(k_{z,n_z})$ with the defined positions of (9) and 1D FFT to the order difference $m-n$ respectively, $\sigma^{qp}_{mn}(k_{z,n_z})\, a_n^{S\alpha}(k_{z,n_z})$ can be computed as

$$\tilde{\boldsymbol{\psi}}^{\alpha} = FFT^{-1}\left\{\boldsymbol{\sigma}_{\mathbf{F}} \circ \mathbf{a}^{\mathbf{S\alpha}}_{\mathbf{F}}\right\}. \tag{11}$$

The key point of 2D-SMCG-FFT is a translation of the random positions $\bar{\rho}_q$ to a periodic grid so that 2D FFT can be applied to periodic grid points [26]. Note that the computation of (10) requires a three-step procedure to respond to randomly positioned trees [22]: (i) pre-multiplication (ii) triple FFT and (iii) post-multiplication. The third FFT is new, and is due to the order of the vector cylindrical waves.

Using the translational addition theorem, the Foldy-Lax equation transforms into the following form

$$\begin{aligned}
a^{E\beta}_{m,q}(k_z) = a^{I\beta}_{m,q}(k_z) + \sum_{p=1,p\neq q}\sum_n H^{(1)}_{m-n}(k_\rho|\bar{\rho}_{pq}|)\\
\times e^{-i(m-n)\phi_{\overline{\rho_p\rho_q}}} e^{-ik_z(z_p-z_q)} a^{S\beta}_{n,p}(k_z).
\end{aligned} \tag{12}$$

The coupling of VCW order m of scatterer q is coupled to VCW order n of scatterer p through the order difference of $m-n$, as shown in the above equation. This allows FFT on the order of VCW so that the computation is $N_{\max}\log N_{\max}$ instead of $N^2_{\max}$, where $N_{\max}$ is the maximum order of VCW.

The CPU time and the memory of the FHM follow $O\left(N_qN_n^2N_m^2 + N_mN_qN_{sn}\log N_qN_{sn}\right)$ and $O(N_TN_n^2N_m^2 + N_mN_qN_n)$, where N_T is the number of T-matrices (different T-matrices corresponding to different trees) and N_q is the number of scatterers. In the CPU time complexity, the first term in the big O notation, $N_qN_{sn}^2N_m^2$, is associated with

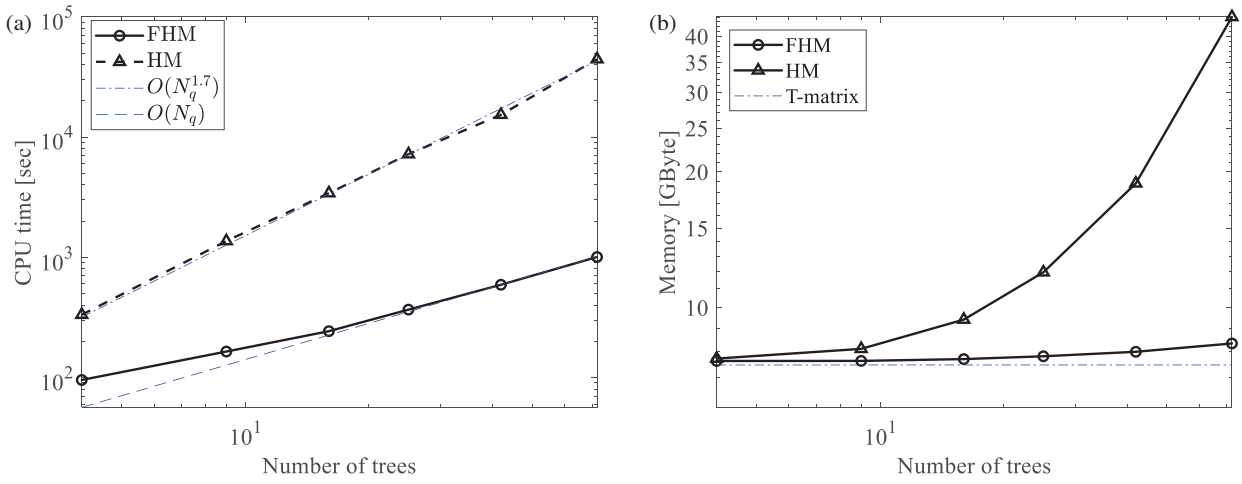

FIGURE 3. Computational efficiency of the FHM: (a) CPU time and (b) memory.

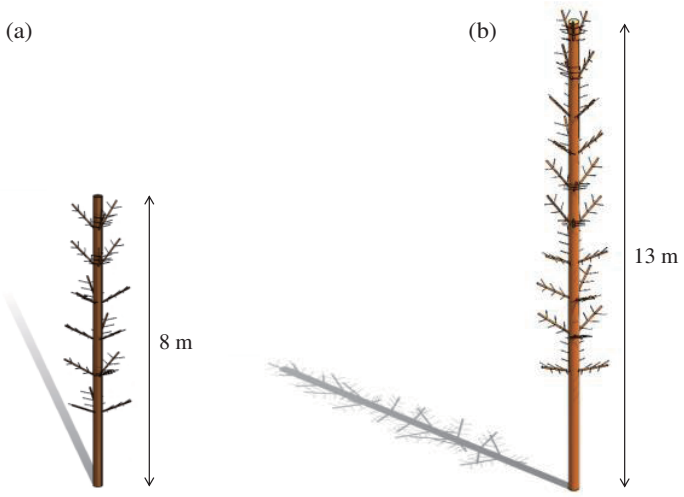

FIGURE 4. 3-D modeling of (a) eight m height tree and (b) 13 m height tree.

T-matrix multiplication. The second term related to triple FFT, $N_m N_q N_{sn} \log N_q N_{sn}$, increases smoothly due to the logarithmic nature of N_q.

To obtain the requirements of CPU time and the memory, the FHM is performed on the desktop computer of Intel Core i7-10700 CPU and 32 GB RAM. The CPU time and memory usage, as shown in Figs. 3(a) and (b), respectively, are measured by increasing the number of identical trees ($N_t = 1$) and calculating scattered fields using an iterative solution order of 2. The large number of trees used in this paper is 72 trees.

We compare the FHM and the HM used in [21]. In Fig. 3(a), it can be observed that between 9 and 16 trees, the estimated order is different from that of the FHM due to additional computational tasks such as uploading T-matrix and generating the translation addition terms. However, as the computational complexity of solving the system of linear equations becomes dominant, the order of the computational time matches that of the FHM after 16 trees. The computational complexity shows that $O(N_q)$ is dominant when N_q less than 72 as shown in Fig. 3(a), whereas the hybrid method shows $O\left(N_q^{1.7}\right)$. Note that in cases where $\log(N_q N_{sn})$ is larger than $N_n N_m$, it follows $O(N_q \log N_q)$. The memory usage of the FHM remains at the level of the T-matrix memory as shown in Fig. 3(b), whereas the HM significantly increases due to the need to store the σ matrix [22].

3. VALIDATION OF THE FHM: 8 M AND 13 M HEIGHT TREES

In this section, we will implement the FHM procedure to generate full-wave simulations of trees. The numerical solutions are validated by comparisons with commercial software FEKO. We consider two tree heights: 8 meters and 13 meters. The structures of the 8 m and 13 m trees are depicted in Fig. 4, and the dimensions and the numbers of their trunks and branches are presented in Table 2. The primary branches on each layer are

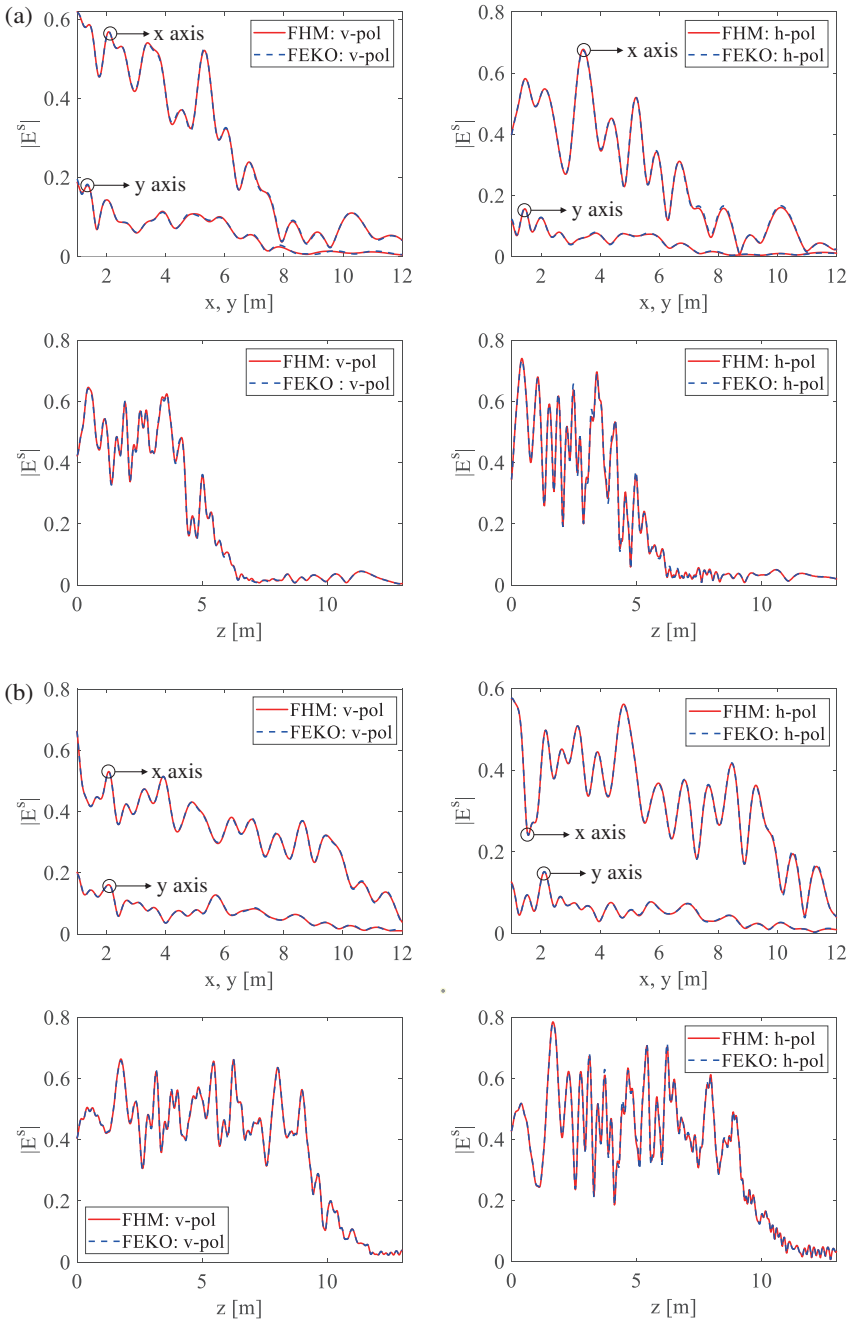

FIGURE 5. T-matrix validation: comparison of scattered fields between the FHM and FEKO. In FHM, we first extract the T-matrix and then use the T-matrix to calculate the scattered fields. (a) 8 m height tree (a single tree), (b) 13 m height tree (a single tree).

TABLE 2. Number and dimensions of a trunk and branches.

	Trunk	Primary Branch	Secondary Branch
Number	1	30 (18)	180 (108)
Length [m]	13 (8)	1	0.3
Radius [cm]	12.5	2	0.5

(): 8 m tree

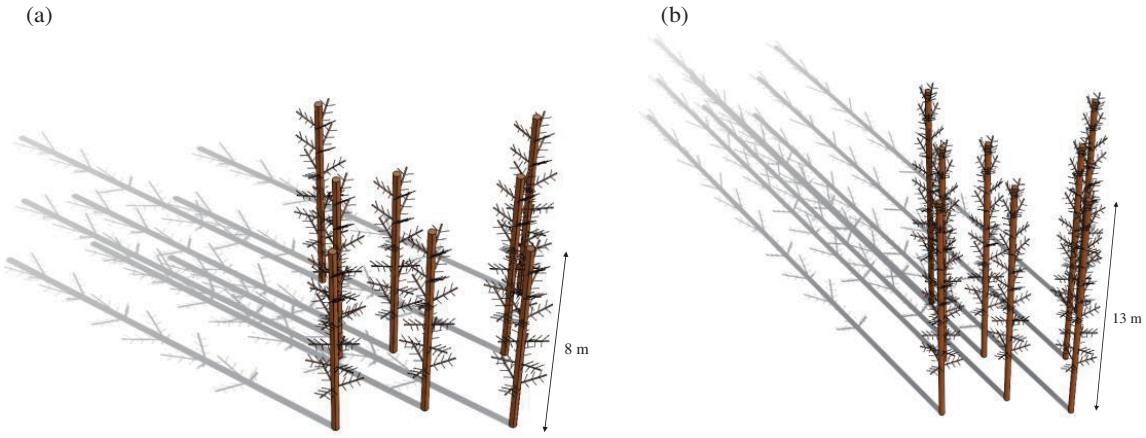

FIGURE 6. Geometric configuration for validation scenarios. Trees used in both scenarios are positioned in the same locations. (a) 8 trees: 8 m height, (b) 8 trees: 13 m height.

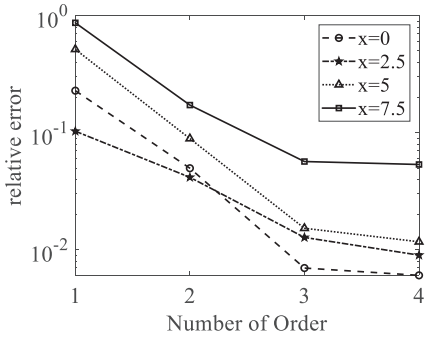

FIGURE 7. Order of iterative solutions: convergence of iterative solutions is attained at the 4th order. The field points are located on the parallel to x-axis at $y = 1.5$ m, $z = 0$ m.

rotated with respect to azimuthal angles. The bottom plane of the trees is denoted by $z = 0$. The trees consist of dielectric materials. The permittivity of trees throughout this paper is set to $13.68 + 4.62i$.

3.1. Validation of T-Matrix

Far-field bistatic scattering amplitude solutions are obtained by FEKO [32], which is used to extract the T-matrix of VCWs. To validate the T-matrix in the FHM, we compare the electric fields obtained from the FHM with those from FEKO. Specifically, we obtain the scattered fields directly from FEKO using a single tree, while for the FHM, we compute the electric fields using vector cylindrical waves and their associated scattering coefficients from (3).

The VCW functions utilized in the FHM employ a total of 267 set k_z sampling points, representing z-directional wave components (Nm), and 41 azimuthal modes (Nn) equivalent to $N_{\max} = 20$. The extracted two T-matrices are validated by comparing scattered fields of FEKO to that of the FHM as shown in Figs. 5(a) and (b), where the field points of the scattered fields are located on the x-, y-, and z-axes, respectively. The incident plane waves are polarized vertically and horizontally, corresponding to $E_{vi} = 1$, $E_{hi} = 0$ and $E_{vi} = 0$, $E_{hi} = 1$ in (6), respectively, with $\theta_i = 140°$ and $\phi_i = 0°$. Note that the vector points outward from the origin: θ_i is an angle between the z-axis and a vector, and ϕ_i is an azimuth between the x-axis and a vector projected on a x-y plane. Thus, a downward going wave with a negative z-component is at θ_i equal to 140 degrees that make an angle of 40 degrees with the negative z-axis. The incidence angle of the SMAP observations is 40 degrees [33]. These incident waves are used through this paper. The two solutions obtained from using FEKO and the FHM exhibit excellent agreement. These agreements validate the accuracy of the extracted T-matrices. The obtained T-matrices are put in a library as they are re-useable for various simulation cases.

3.2. Validations of Multiple Scattering solutions of FHM

In this sub-section, we validate the fast multiple scattering solutions based on the Foldy-Lax equation. As shown in Figs. 6(a) and (b) the validation scenarios involve the use of eight trees to compare with FEKO. The scenarios consist of eight randomly positioned trees with gaps between each other. The scenarios involving eight m and 13 m high trees use the same positions. We check the iterative order in (9) before generating the scattered fields. The relative error defined as relative error $= \left\| E^{(i)}_{FHM} - E_{FEKO} \right\|_F / \left\| E_{FEKO} \right\|_F$ where (i) denotes an order of iteration. Convergence is observed at the 4$^{\text{th}}$ order of multiple scattering as shown in Fig. 7.

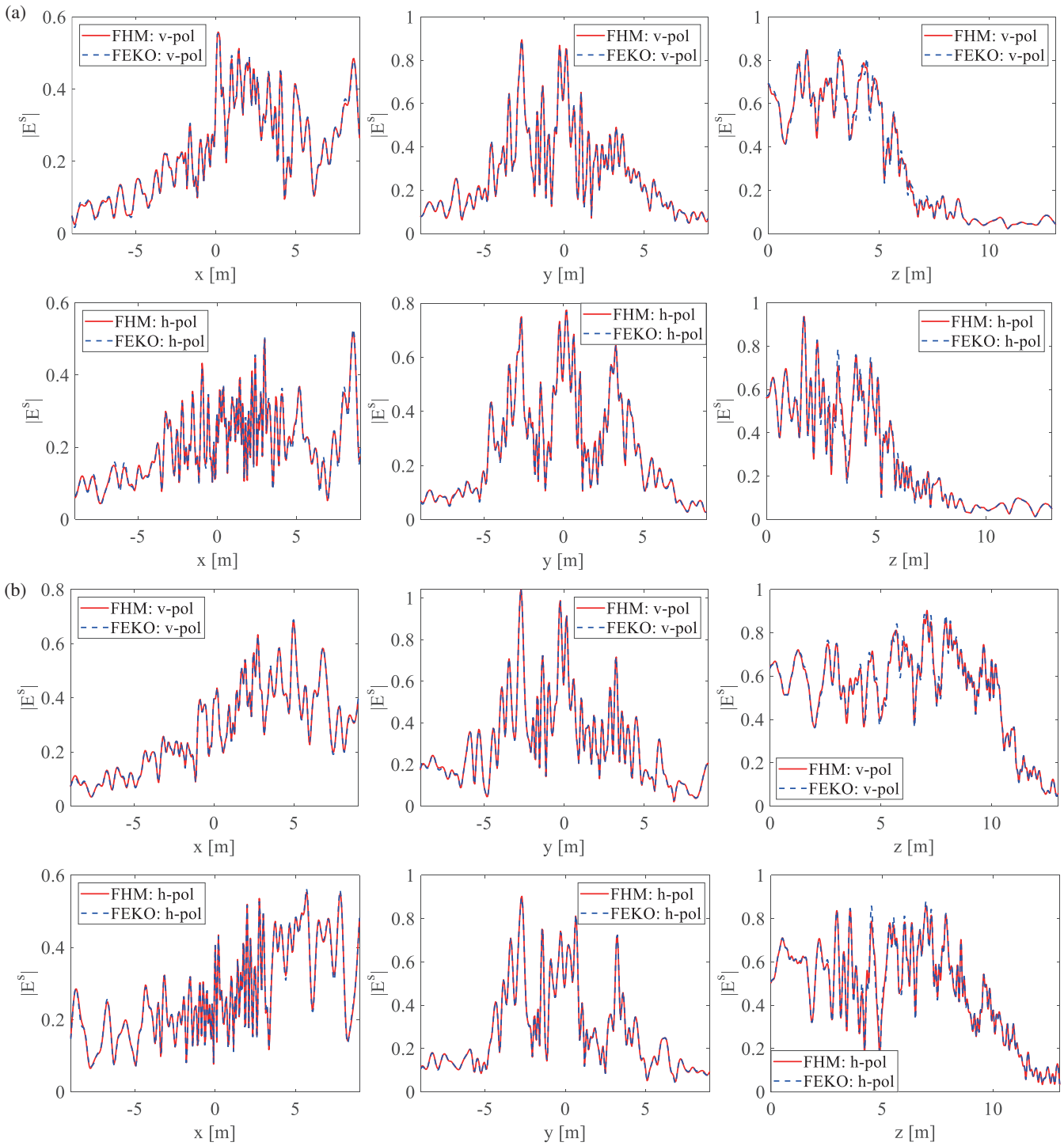

FIGURE 8. Validation of multiple scattering solutions of FHM. (a) 8 trees: 8 m height, (b) 8 trees: 13 m height.

The scattered fields from eight trees are generated by performing the fast multiple scattering computation. The vertically and horizontally polarized incident waves are used in each simulation, respectively. The field points for Figs. 8(a) and (b) are along the x-axis such that $-10\,\text{m} \leq x \leq 10\,\text{m}$, $y = 1.5\,\text{m}$, $z = 0\,\text{m}$, along the y-axis such that $x = 1.5\,\text{m}$, $-10 \leq y \leq 10\,\text{m}$, $z = 0\,\text{m}$, and along the z-axis such that $x = 1.5\,\text{m}$, $y = 0\,\text{m}$, $0 \leq z \leq 13\,\text{m}$. The scattered fields obtained from the FHM and FEKO simulations show good agreement. We calculate the spatial distributions of fields at the bottom plane $z = 0\,\text{m}$ (underneath the trees). The solutions are compared to those obtained from FEKO. The electric and magnetic fields at the bottom will be used to compute transmissivity in the next section. Two results shown in Figs. 9(a) and (b), exhibit good agreement with FEKO. The fields in Fig. 9 are equal to unity on the left region because the incident waves in that region do not encounter any trees. In the right region, the amplitudes of the electric fields can be larger than the unity meaning

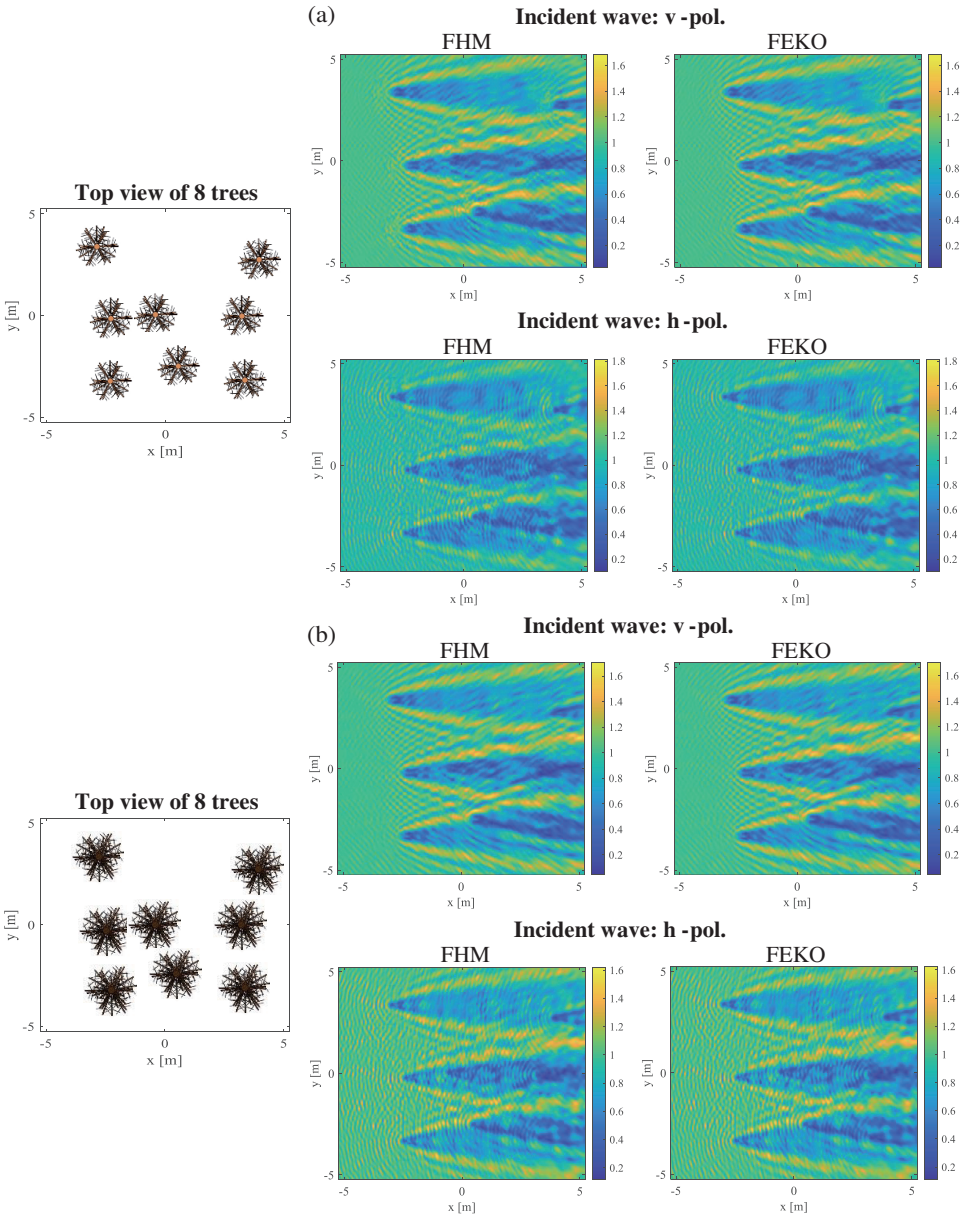

FIGURE 9. Total fields on the bottom plane. (a) 8 m height tree, (b) 13 m height tree.

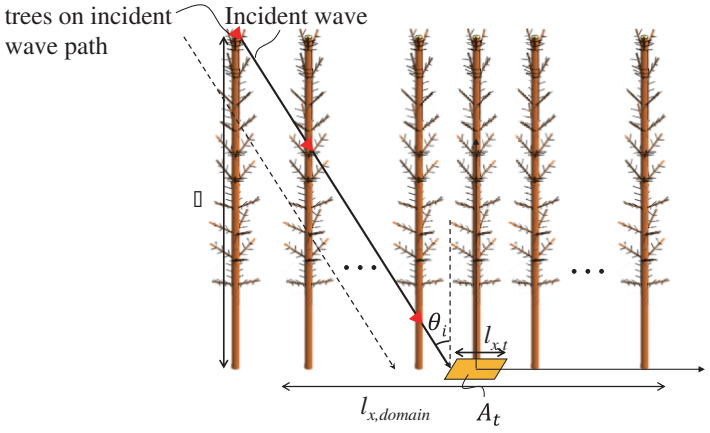

FIGURE 10. Two areas of transmissivity computation: A_t and A_{domain}.

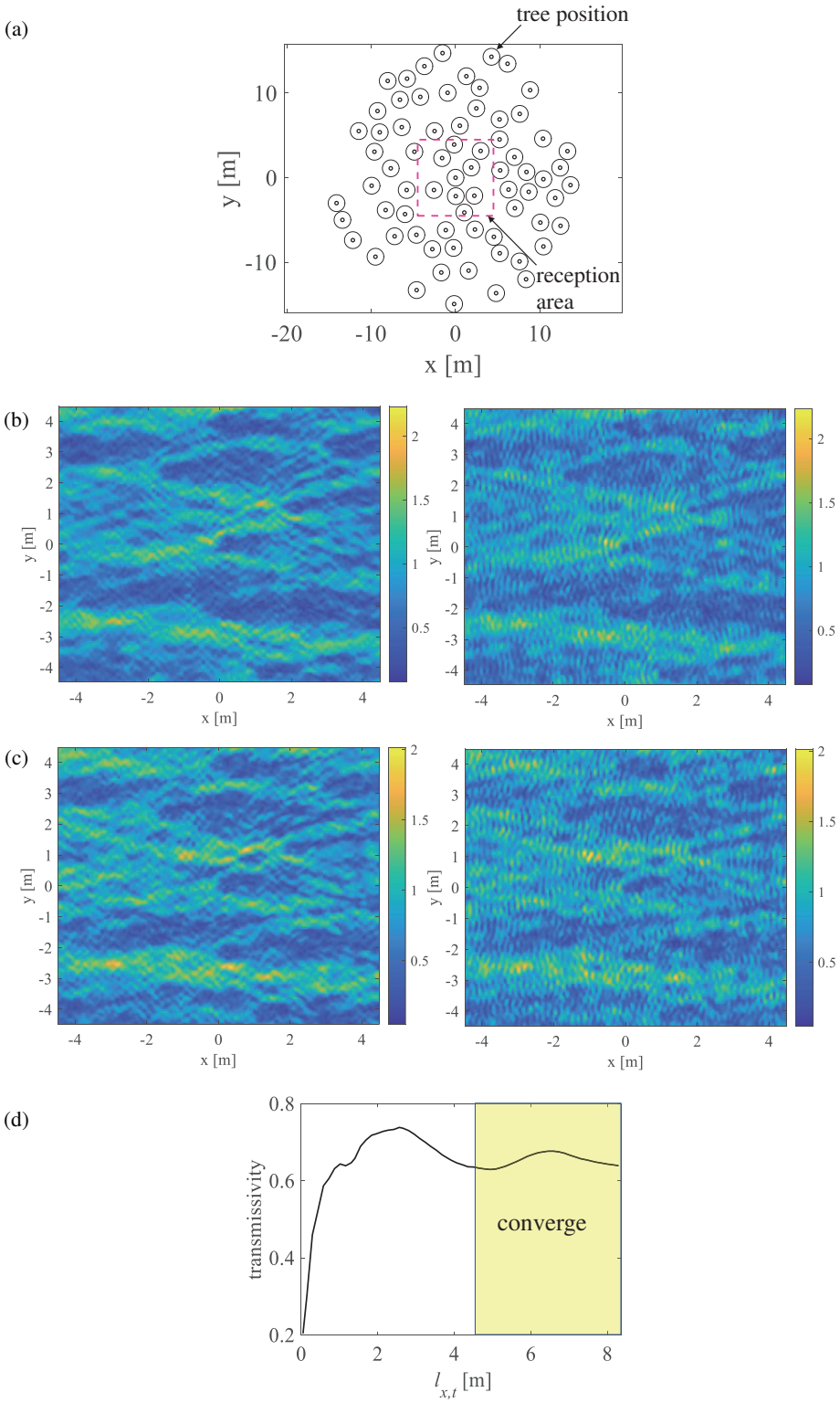

FIGURE 11. Full-wave simulations of forest of 72 trees. (a) Randomized positions of trees, (b) 8 m height: spatial electric field distributions on the reception area by vertically polarized (left) and horizontally polarized incident plane waves (right), respectively, (c) 13 m height: spatial electric field distributions on the reception area by vertically polarized (left) and horizontally polarized incident plane waves (right), respectively, (d) convergent values of transmissivity with respect to $l_{x,t}$.

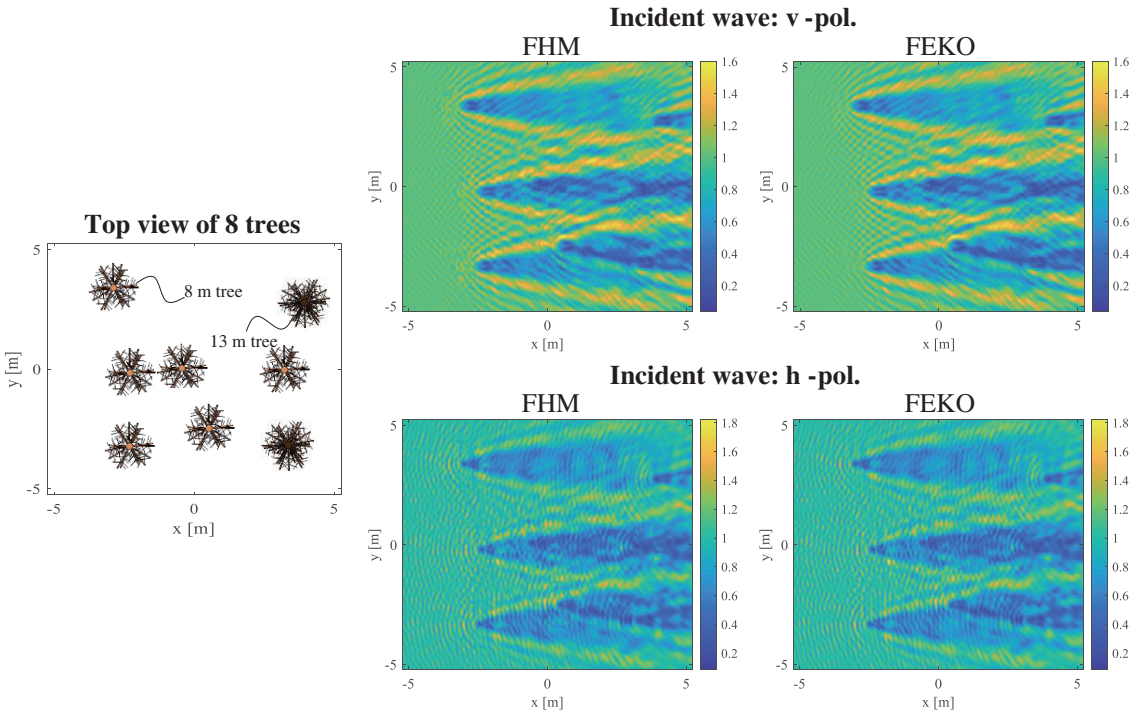

FIGURE 12. Validation of 8 mixed height trees where the height of a tree is either 8 m or 13 m.

that they are greater than those of incident waves. The values larger than unity are a result of constructive interference. The blue regions in Figs. 9(a) and (b) represent the shadowed areas where the incident waves are attenuated by the trees, resulting in electric field values less than unity. The advantage of full-wave simulations is that they give constructive and destructive interference of electric field distributions in forested areas. Notably, (i) the average Poyning's vector and the average transmissivity are less than unity due to energy conservation, and (ii) the radiative transfer theory only gives an average (based on the statistical homogeneity assumptions discussed earlier). The results of Fig. 9 show "edge effects" meaning the fields on the periphery of the simulation domain area do not have the correct random media effects. We shall eliminate edge effects in our subsequent forest simulations. Fig. 9 shows comparable magnitudes of vertical and horizontal polarizations which are in the results of both FEKO and FHM. Note that using a small number of trees such as eight trees is merely for validation of the FHM against FEKO. For applications considered here the results of simulations of eight trees are useless and meaningless as there are too much edge/gap effects. A group of trees with a representative density is needed to focus on the group's interior domain to avoid edge effects.

4. FULL-WAVE ELECTROMAGNETIC SIMULATION OF FORESTS

This section applies the FHM to full-wave electromagnetic simulations of forests. The forests are shown in Figs. 1(a) and (b) with a forest area of about 714 m^2. The tree density of the forests is set to 0.1 tree/m^2, giving 72 trees in the forest. The incident waves are the same as used in the previous section. Forests in Figs. 1(a) and (b) are generated by randomized process considering the forest area $A_{domain} = \pi \left(d_{domain}/2\right)^2$, where d_{domain} is the forest diameter. The tree position q is randomly selected by

$$\bar{\rho}_q = R\cos\Psi\hat{x} + R\sin\Psi\hat{y}$$

where the ranges of two random variables are $0 \leq R \leq d_{domain}/2$ and $0 \leq \Psi \leq 2\pi$, respectively, and they follow the uniform distribution.

To investigate the penetration of microwaves through forested environments, it is necessary to design a simulation scheme. To capture the multiple scattering effects of trees, we must include many trees and eliminate edge effects. We define two regions: a domain area A_{domain} and a reception (test) area A_t. The domain encompasses the region where all 72 trees are situated, and within this area, we compute the multiple scattering effects of these 72 trees. The reception (test) area is the region we use to illustrate the field distributions and the transmissivity. Our design is such that $A_t \ll A_{domain}$ so that A_t does not have edge effects. As shown in Fig. 10, the incident plane waves pass through trees, and they reach A_t. The trees on this path of the incident waves should be included in the A_{domain}. Otherwise, the incident waves directly hit A_t leading to an edge effect, which means that the discontinuity of trees on the edge increases transmitted power. With these considerations, we have the design parameter as shown below,

$$d_{domain} = l_{x,t} + 2h\tan\theta_i \tag{13}$$

where h and $l_{x,t}$ are the tree height and the side length of A_t, respectively. As discussed in [24], since using a large reception area can reduce the number of realizations in Monte Carlo

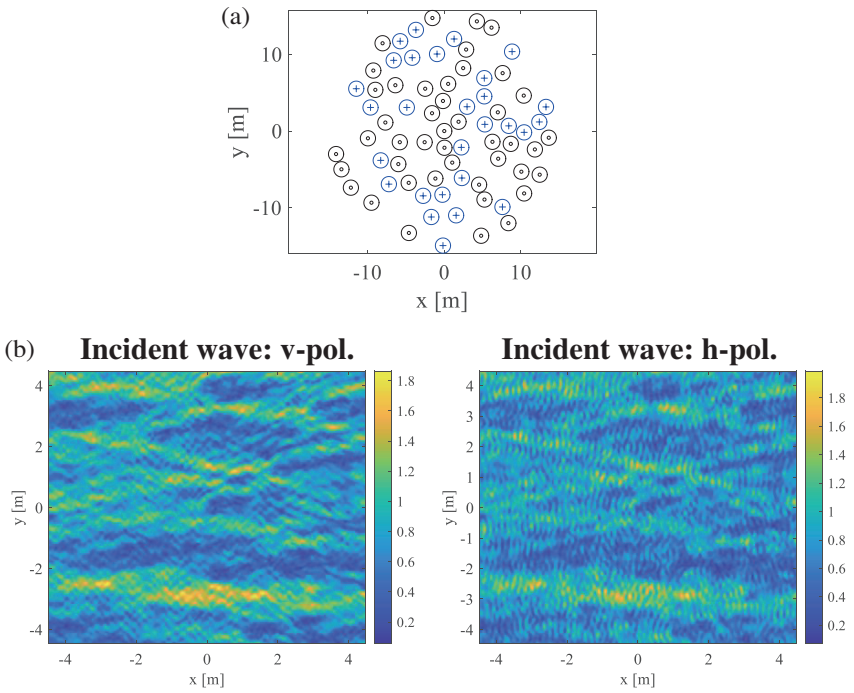

FIGURE 13. Electromagnetic simulations of forest of mixed trees: (a) geometric configuration (circle: 13 m tree, cross: 8 m tree), (b) electric field distributions.

simulations, $l_{x,t}$ is set to around 40 wavelengths, and as a result d_{domain} is 30.16 m. The correctness of this design scheme can be tested by increasing A_{domain} and A_t until convergence of transmissivity is obtained.

Based on this design scheme, we generate the geometric configuration of a forest of 72 trees as shown in Fig. 11(a). Spatial electric field distributions on the reception area, illustrated in Figs. 11(b) and (c), are computed using the multiple scattering solutions. Based on electromagnetic waves on the bottom plane, we compute the transmissivity from the Poynting vector as shown below,

$$T = \frac{1}{A_t} \iint_{A_t} \frac{\bar{S}^{tot} \cdot (-\hat{z})}{\bar{S}^{inc} \cdot (-\hat{z})} d\bar{r}. \tag{14}$$

By increasing the parameter $l_{x,t}$, the transmissivity is computed for each corresponding value of $l_{x,t}$. This process allows us to observe the convergent behavior of the transmissivity, as shown in Fig. 11(d), where the transmissivity converges to a value of approximately 0.639. As shown in Figs. 11(b) and (c), we eliminate edge effects for area A_t due to the design scheme using two areas A_{domain} and A_t. The electric fields shown in Fig. 11(b) and (c) can be as high as twice the incident wave. Taking the absolute value square to obtain the power means that the highest Poynting vector can be four times that of the incident wave. The spatial field distributions show that the fields are unevenly distributed with large fields in the gap region and smaller fields in the shadow region. The ratio of field maxima and minima can be very high. This is the advantage of full-wave simulations while the radiative transfer theory only gives one number, viz. the average Poynting's vector. The Foldy-Lax equation is solved up to the 4$^{\text{th}}$ order of wave scattering. Table 3 shows the CPU time and the memory required for the computation performed on a desktop computer; the CPU time is measured for one realization. The CPU time is merely 22.5 minutes, and the required memory is merely 16.5 GB.

4.1. Forest of Trees with Mixed Heights

To simulate a case corresponding to trees with varying heights in the forest, the FHM is applied to forests comprising of randomly selected trees ranging between eight m and 13 m. We use two random sets of positions and varying tree heights. The FHM utilizes pre-stored T-matrices of eight m and 13 m trees from a library, allowing it to efficiently solve multiple scattering problems by reusing those T-matrices. Before implementing full-wave electromagnetic simulations of many trees, we validate the scenario of the eight mixed height trees. The positions of trees corresponding to two heights are shown in Fig. 12. The total fields of the FHM results agree with those of FEKO. We further increase the number of trees to 72, as depicted in the geometric configuration shown in Fig. 13(a). We utilize the tree location profile depicted in Fig. 11(a) to compute the spatial electric field distributions on the reception area using the FHM, as shown in Fig. 13(b).

To calculate transmissivities of randomly positioned trees and randomly selected tree heights (mixed height trees), we perform Monte Carlo simulations involving averaging the transmissivities across multiple realizations as shown below [25],

$$t = \frac{1}{N} \sum_{n=1}^{N} T_n \tag{15}$$

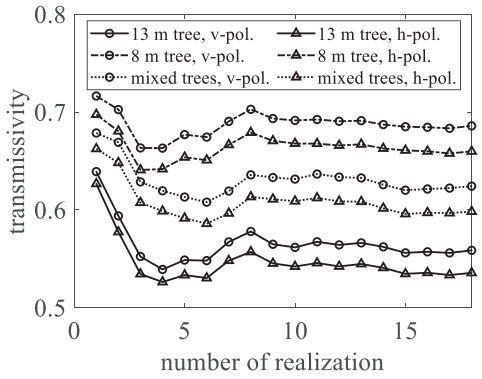

FIGURE 14. Monte Carlo simulations of transmissivities with randomly positioned trees.

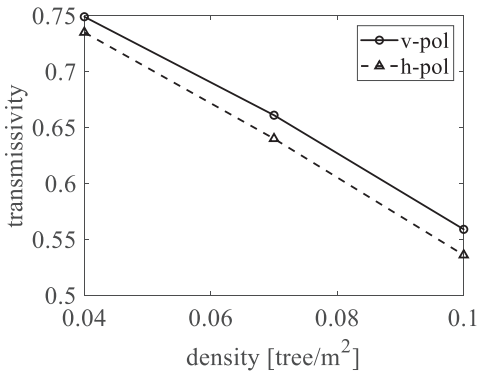

FIGURE 15. Transmissivities of different tree densities: 13 m tall tree.

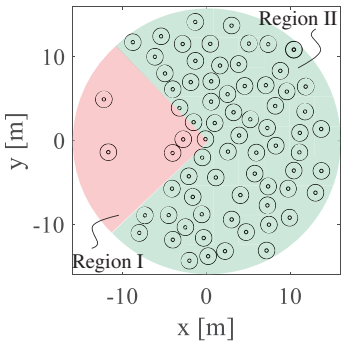

FIGURE 16. Non-uniform distribution of trees (a cluster of trees). The number of trees is 72.

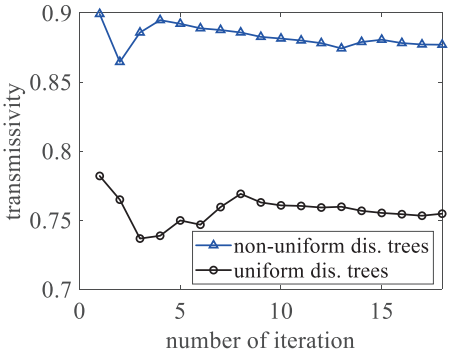

FIGURE 17. Comparison of transmissivities between non-uniform distributions of trees (a cluster of trees) and uniform distributions of trees.

TABLE 3. CPU time and memory usage for simulating 72 trees using 4th order iterative solutions on a desktop computer equipped with an Intel Core i7-10700 CPU and 32 GB of RAM.

# of Trees	CPU time	Memory
72	1346 sec.	16.5 GB

TABLE 4. Transmissivity of forest.

Scenario	13 m trees	8 m trees	13 m and 8 m mixed trees
v-pol.	0.559	0.686	0.624
h-pol.	0.536	0.660	0.598

TABLE 5. Number and dimensions of a trunk and branches: Non-uniform distribution of trees.

	Trunk	Primary Branch	Secondary Branch
Number	1	18	108
Length [m]	8	1	0.3
Radius [cm]	2	2	0.5

where T_n is a realization corresponding to the n-th random set of tree positions. Each realization is generated by randomly assigning positions to the trees in the simulation domain as described in the Section 4. The random variables of tree heights also follow the uniform distribution. We apply this procedure to the forests of eight m trees, 13 m trees, and mixed trees, respectively, and compare them with each other. Fig. 14 presents the transmissivity results for incident waves with vertical and horizontal polarizations, respectively. As the number of realizations increases, the transmissivities converge. At the L-band, the transmissivities obtained from vertically polarized incident waves show higher values in comparison to those obtained from horizontally polarized waves. As the numbers of the 13 m trees and 8 m trees used in the mixed tree scenario are approximately equal it is logical that the transmissivities of the mixed trees fall between those of the 13 m trees and the eight m trees. The transmissivities are summarized in Table 4. The tree densities in natural forests vary; Fig. 15 shows transmissivities as a function of tree density. As expected, the transmissivity decreases with increasing density.

4.2. Nonuniform Distributions of Trees

The various tree clustering patterns result in distinct transmissivities. This is in contrast to the RTE which gives the same result with or without clustering if the average number of trees per unit area is the same. Note that the RTE assumes that the scatterers are uniformly distributed across the region. To investigate a significant effect of tree clusters on transmissivies, trees are randomly generated as shown in Fig. 16. The trees are more open on the left side due to a lower tree density on that side: Region I and Region II exhibit tree densities of 0.0224 trees/m^2 and 0.127 trees/m^2, respectively, and the overall average tree density maintains the same 0.1 trees/m^2 with that of the uniform distributions. Note that this condition increases the transmissivity difference between non-uniform and uniform distributions of trees. Two regions are defined by two ranges of angles: Region I is $S_I \in [3\pi/4, 5\pi/4]$ and Region II is $S_{II} \in [5\pi/4, 11\pi/4]$. In the FHM, a non-uniform medium is composed of slender-trunk trees whose dimensions are described in Table 5. The transmissivity of the tree cluster is compared to that of the uniform distribution, as illustrated in Fig. 17. Due to the cluster effect, the transmissivity is larger than that of the uniform distributions. Therefore, the full-wave simulation results indicate that the various geometric configurations lead to distinct transmissivities although the overall tree density is the same.

5. CONCLUSIONS

In this paper, we perform full-wave electromagnetic simulations of forests at L-band. Due to accuracy and efficient solutions of electromagnetic wave propagation through forest, the FHM is beneficial for full-wave electromagnetic simulations of forests. The FHM maintains low computational complexity as the number of trees increases, which enables us to simulate wave scattering of 72 trees in simulation domain. We show that the FHM based on the triple FFT technique is highly efficient to solve wave scattering of trees within 1346 sec and 16.5 GB on the desktop. The validation of the FHM is confirmed through comparisons with FEKO results, demonstrating a high level of agreement between the two. We design the simulation domain and calculate the electric field distributions underneath forest. Using forests of 8 m and 13 m trees, the FHM is successfully applied to calculate the solutions. The electric field distributions are uneven at the bottom plane of the trees with large amplitudes at twice that of the incident wave so that the highest Poynting vector can be 4 times that of the incident wave. The transmissivity of 13 m trees is about 0.56 and that of eight m trees is about 0.69. The scenario involving a mixture of trees with heights of 8 m and 13 m shows that the transmissivity falls between the values corresponding to the 13 m trees and the 8 m trees. The FHM shows that the L-band microwave signals of the SMAP mission can penetrate forests of larger than 5 kg/m^2. Based on the significant field strength observed in the field distribution, we conclude that targets concealed under forests can be detected. Similarly, in wireless communication, GPS signals beneath forest cover are successfully received. We show that the full-wave simulations provide different transmissivities depending on distributions of trees. The results of transmissivities vary with clustering and without clustering of trees. The CPU time of FHM can be further improved by such as using the method of steepest descents to approximate the far-distance wave interaction of trees. The ongoing work aims to combine the FHM with the rough surface at the bottom of the trees.

ACKNOWLEDGEMENT

The research described in this paper was carried out at the University of Michigan, Ann Arbor and was supported in part by the Jet Propulsion Laboratory, California Institute of Technology, under a contract with the National Aeronautics and Space Administration (NASA), and in part by the NASA SMAP Program and the NASA Remote Sensing Theory Program. The authors thank Altair Engineering for granting the full version of FEKO to the Radiation Laboratory of the University of Michigan.

REFERENCES

[1] Jiang, S., Q. Zhu, C.-X. Wang, *et al.*, "Map-based UAV mmWave channel model and characteristics analysis," in *2020 IEEE/CIC International Conference on Communications in China (ICCC Workshops)*, 23–28, Chongqing, China, Aug. 2020.

[2] Le Palud, M., T. Dupaquier, and L. Bertel, "Experimental study of VHF propagation in forested environment and modelling techniques," in *Record of the IEEE 2000 International Radar Conference*, 539–544, Alexandria, VA, USA, May 2000.

[3] Le Palud, M., "Propagation modeling of VHF radio channel in forest environments," in *IEEE MILCOM 2004. Military Communications Conference*, Vol. 2, 609–614, Monterey, CA, USA, Oct. 2004.

[4] Davis, M. E., "Developments in foliage penetration radar," in *2009 International Radar Conference "Surveillance for a Safer World" (RADAR 2009)*, 1–6, Bordeaux, France, 2009.

[5] Vint, D., M. Anderson, Y. Yang, C. Ilioudis, G. D. Caterina, and C. Clemente, "Automatic target recognition for low resolution foliage penetrating SAR images using CNNs and GANs," *Re-*

mote Sensing, Vol. 13, No. 4, 596, Feb. 2021.

[6] Jaramillo, M. R., "Computational electromagnetic modeling (CEM) of foliage penetration (FOPEN)," Ph.D. dissertation, Electrical and Computer Engineering, University of New Mexico, 2021.

[7] Kim, J., I.-S. Koh, and Y. Lee, "Simulation of passive time-reversal surveillance system for detection of target invasion inside forested environment," in *2016 International Symposium on Antennas and Propagation (ISAP)*, 318–319, Okinawa, Japan, Oct. 2016.

[8] Oré, G., A. Santos, D. Ukan, *et al.*, "Ant nests detection in industrial forests by SAR P-band tomography," in *2022 IEEE International Geoscience and Remote Sensing Symposium (IGARSS 2022)*, 4791–4794, Kuala Lumpur, Malaysia, Jul. 2022.

[9] Colliander, A., M. H. Cosh, A. Berg, *et al.*, "Development of SMAP retrievals for forested regions: SMAPVEX19-22 and SMAPVEX22-Boreal," in *2022 IEEE International Geoscience and Remote Sensing Symposium (IGARSS 2022)*, 4228–4231, Kuala Lumpur, Malaysia, Jul. 2022.

[10] Liao, T.-H. and S.-B. Kim, "Dual-frequency retrieval of soil moisture from L- and S-band radar data for corn and soybean," *Remote Sensing*, Vol. 14, No. 22, 5875, Nov. 2022.

[11] Park, J., R. Bindlish, A. Bringer, D. Horton, and J. T. Johnson, "Soil moisture retrieval using a time-series ratio algorithm for the NISAR mission," in *2021 IEEE International Geoscience and Remote Sensing Symposium IGARSS*, 5873–5876, Brussels, Belgium, 2021.

[12] Siqueira, P., J. Armston, B. Chapman, *et al.*, "Ecosystem sciences with NISAR," in *2021 IEEE International Geoscience and Remote Sensing Symposium IGARSS*, 547–549, Brussels, Belgium, 2021.

[13] Liu, D., Y. Du, G. Sun, W.-Z. Yan, and B.-I. Wu, "Analysis of InSAR sensitivity to forest structure based on radar scattering model," *Progress In Electromagnetics Research*, Vol. 84, 149–171, 2008.

[14] Campbell, J. D., R. Akbar, A. Bringer, *et al.*, "Intercomparison of electromagnetic scattering models for Delay-Doppler maps along a CYGNSS land track with topography," *IEEE Transactions on Geoscience and Remote Sensing*, Vol. 60, No. 2007413, 1–13, Sep. 2022.

[15] Unwin, M. J. and othersl, "An introduction to the HydroGNSS GNSS reflectometry remote sensing mission," *IEEE Journal of Selected Topics in Applied Earth Observations and Remote Sensing*, Vol. 14, 6987–6999, 2021.

[16] Camps, A., A. Alonso-Arroyo, H. Park, R. Onrubia, D. Pascual, and J. Querol, "L-band vegetation optical depth estimation using transmitted GNSS signals: Application to GNSS-reflectometry and positioning," *Remote Sensing*, Vol. 12, No. 15, 2352, Aug. 2020.

[17] Colliander, A., R. H. Reichle, W. T. Crow, *et al.*, "Validation of soil moisture data products from the NASA SMAP mission," *IEEE Journal of Selected Topics in Applied Earth Observations and Remote Sensing*, Vol. 15, 364–392, 2022.

[18] Ulaby, F. T., K. Sarabandi, K. McDonald, M. Whitt, and M. C. Dobson, "Michigan microwave canopy scattering model," *International Journal of Remote Sensing*, Vol. 11, No. 7, 1223–1253, Jul. 1990.

[19] Lang, R. H. and J. S. Sighu, "Electromagnetic backscattering from a layer of vegetation: A discrete approach," *IEEE Transactions on Geoscience and Remote Sensing*, Vol. 21, No. 1, 62–71, Jan. 1983.

[20] Gu, W., L. Tsang, A. Colliander, and S. H. Yueh, "Multi-frequency full-wave simulations of vegetation using a hybrid method," *IEEE Transactions on Microwave Theory and Techniques*, Vol. 70, No. 1, 275–285, Jan. 2022.

[21] Gu, W., L. Tsang, A. Colliander, and S. Yueh, "Hybrid method for full-wave simulations of forests at L-band," *IEEE Access*, Vol. 10, 105 898–105 909, 2022.

[22] Jeong, J., L. Tsang, W. Gu, A. Colliander, and S. H. Yueh, "Wave propagation in vegetation field by combining fast multiple scattering theory and numerical electromagnetics in a hybrid method," *IEEE Transactions on Antennas and Propagation*, Vol. 71, No. 4, 3598–3610, Apr. 2023.

[23] Huang, H., L. Tsang, E. G. Njoku, A. Colliander, T.-H. Liao, and K.-H. Ding, "Propagation and scattering by a layer of randomly distributed dielectric cylinders using monte carlo simulations of 3D Maxwell equations with applications in microwave interactions with vegetation," *IEEE Access*, Vol. 5, 11 985–12 003, 2017.

[24] Huang, H., L. Tsang, A. Colliander, and S. H. Yueh, "Propagation of waves in randomly distributed cylinders using three-dimensional vector cylindrical wave expansions in foldy-lax equations," *IEEE Journal on Multiscale and Multiphysics Computational Techniques*, Vol. 4, 214–226, Dec. 2019.

[25] Gu, W., L. Tsang, A. Colliander, and S. H. Yueh, "Wave propagation in vegetation field using a hybrid method," *IEEE Transactions on Antennas and Propagation*, Vol. 69, No. 10, 6752–6761, Oct. 2021.

[26] CHAN, C. H. and L. Tsang, "A sparse-matrix canonical-grid method for scattering by many scatterers," *Microwave and Optical Technology Letters*, Vol. 8, No. 2, 114–118, Feb. 1995.

[27] Jeong, J., L. Tsang, X. Xu, S. H. Yueh, and S. A. Margulis, "Full-wave electromagnetic model simulations of P-band radio signal propagation through forest using the fast hybrid method," *IEEE Journal of Selected Topics in Applied Earth Observations and Remote Sensing*, Vol. 16, 6711–6722, Jul. 2023.

[28] Mastorakis, E., P. J. Papakanellos, H. T. Anastassiu, and N. L. Tsitsas, "Analysis of electromagnetic scattering from large arrays of cylinders via a hybrid of the method of auxiliary sources (MAS) with the fast multipole method (FMM)," *Mathematics*, Vol. 10, No. 17, 3211, Sep. 2022.

[29] Blankrot, B. and Y. Leviatan, "FMM-accelerated source-model technique for many-scatterer problems," *IEEE Transactions on Antennas and Propagation*, Vol. 65, No. 8, 4379–4384, Aug. 2017.

[30] Leonor, N. R., T. R. Fernandes, M. G. Sánchez, and R. F. S. Caldeirinha, "A 3-D model for millimeter-wave propagation through vegetation media using ray-tracing," *IEEE Transactions on Antennas and Propagation*, Vol. 67, No. 6, 4313–4318, Jun. 2019.

[31] Tsang, L., J. A. Kong, K.-H. Ding, and C. O. Ao, *Scattering of Electromagnetic Waves: Theories and Applications*, Wiley, 2001.

[32] Altair Feko, Altair Enc, Inc., www.altairhyperworks.com/feko.

[33] Piepmeier, J. R., P. Focardi, K. A. Horgan, *et al.*, "SMAP L-band microwave radiometer: instrument design and first year on orbit," *IEEE Transactions on Geoscience and Remote Sensing*, Vol. 55, No. 4, 1954–1966, Apr. 2017.

[34] Tsang, L., T.-H. Liao, R. Gao, H. Xu, W. Gu, and J. Zhu, "Theory of microwave remote sensing of vegetation effects, SoOp and rough soil surface backscattering," *Remote Sensing*, Vol. 14, No. 15, Aug. 2022.

[35] Lee, W. and D. Jiao, "Fast structure-aware direct time-domain finite-element solver for the analysis of large-scale On-chip circuits," *IEEE Transactions on Components Packaging and Manufacturing Technology*, Vol. 5, No. 10, 1477–1487, Oct. 2015.